J. Membrane Biol. 188, 199–212 (2002)
DOI: 10.1007/s00232-001-0188-9

The Journal of
Membrane
Biology

Wavelet Analysis of Nonequilibrium Ionic Currents in Human Heart Sodium Channel (hH1a)

A. Hosein-Sooklal, A. Kargol*
Tulane University, Physics Department, New Orleans, LA 70118, USA

Received: 29 January 2002/Revised: 6 May 2002

Abstract. Nonequilibrium response spectroscopy (NRS), the technique of using rapidly fluctuating voltage pulses in the study of ion channels, is applied here. NRS is known to drive an ensemble of ion channels far from equilibrium where, it has been argued, new details of ion channel kinetics can be studied under nonequilibrium conditions. In this paper, a single-pulse NRS technique with custom-designed waveforms built from wavelets is used. The pulses are designed to produce different responses from two competing models of a human heart isoform of the sodium channel (hH1a). Experimental data using this new type of pulses are obtained through whole-cell recordings from mammalian cells (HEK 293). Wavelet analysis of the model response and the experimental data is introduced to show how these NRS pulses can aid in distinguishing the better of the two models and thus introduces another important application of this new technique.

Key words: Sodium ion channel — Markov model — Gating kinetics — Nonequilibrium response spectroscopy — Wavelet transform

Introduction

Towards the beginning of the last century scientists began to investigate means of measuring the physical characteristics of cells and cell membranes. One of the first electrical measurements was made by Fricke and Morse (1925) when they determined a value for the cell membrane capacitance, the value that is presently accepted as a standard. Later, Cole and Curtis (1936) succeeded in measuring the membrane resistance. However, it was not until the voltage-clamp technique was introduced (Marmont, 1949), that the electrical properties of ions flowing through the ion channel pores in the membrane were measured and investigated. This became a very important scientific tool and revolutionized the study of ion channels at that time, as seen from the work of Hodgkin and Huxley (1952*a*,*b*,*c*,*d*) and Hodgkin, Huxley and Katz (1949, 1952). There have since been many modifications and improvements of the method, but the most successful is the patch-clamp technique (Neher & Sakmann, 1976), which allowed recordings from tiny patches of the membrane, using a fire-polished pipette and the formation of a gigaseal (Hamill et al., 1981). This technique was used to make the first single-channel recording and has become a standard technique in ion-channel research. The most common type of voltage protocol used in ion-channel studies has been the step-voltage protocol, in which there is a stepwise change in the transmembrane potential from a set holding potential and where the transient current response to the step is observed and recorded.

In an attempt to better understand, explain and predict the behavior of ion channels, researchers have developed schemes for modeling these protein macromolecules. The basic idea behind these schemes is to describe the possible conformational states and the kinetics between states as the channel switches from an OFF or CLOSED (*C*) position to an ON or OPEN (*O*) position. The modeling of ion channel gating kinetics is an area of continuous research and there have been many different proposals, supported by both theoretical and practical arguments, that claim to be best suited to describe the protein. Among the different schemes, the most commonly discussed are (i) fractal models, (ii) diffusion models, and (iii) discrete Markov models (Colquhoun & Hawkes, 1981; Liebovitch et al., 1987; Korn & Horn, 1988; Milhauser, Salpeter & Oswald, 1988; Liebovitch, 1989; Lowen, Liebovitch & White, 1999). However, the one that has been most commonly used is the discrete Markov model (DMM), mainly because of

Correspondence to: A. Kargol; email: akargol@tulane.edu
*On leave from Physics Institute, Świętokrzyska Academy, 25-406 Kielce, Poland

its clear physical interpretation as well as its ability to fit the experimental data. Discrete Markov models assume that the ion channel molecule has only a discrete number of possible conformations. Physically, the kinetics of the molecule is determined by its energy profile, with the stable conformations corresponding to the energy minima. Obviously, the DMMs do not take into consideration the shape of the energy wells and disregard possible relaxation states within the well. Transitions between the Markov states correspond to thermally activated "jumps" over the potential barriers separating the neighboring wells. It has to be understood that the DMMs are only approximations of the real kinetics of channel molecules and their energy "landscape," but it's an approximation that performed remarkably well in terms of its ability to fit the experimental data.

Discrete Markov models have been used by various research groups to describe different voltage-gated ion channels e.g., the potassium ion channel (Hoshi, Zagotta & Aldrich, 1994; Zagotta, Hoshi & Aldrich, 1994a, Zagotta et al., 1994b; Schoppa & Sigworth, 1998a, 1998b, 1998c) and the sodium ion channel (Hodgkin & Huxley, 1952; Patlak, 1991; Vandenberg & Bezanilla, 1991a, 1991b; Millonas & Hanck, 1998a, 1998b). Each of the models, based on experimental data obtained from whole-cell and single-channel ionic current recordings as well as gating currents, presented a good fit to the ionic current data obtained using stepped-potential protocols. The models, however, have very different topologies, which implies completely different sets of possible conformations of the protein molecule, as well as transitions among them. This ambiguity is a widely acknowledged fact in studies of ion channel-molecule kinetics. Since all of these models are known to fit well the data from stepped-potential protocols, it has been argued (Millonas & Hanck, 1998a; Kargol, Smith & Millonas, 2002b) that currently used experimental protocols have inherent limitations, not related to measurement accuracy, but rather to the type of protocols used.

When stepped-potential protocols are used, the new test potential after the step from the holding potential or from a prepulse is held for a time that is long relative to the longest relaxation time of the channel molecule. In other words, the channel responds to the change in potential during the step, but then is allowed to relax to equilibrium at the test potential. This implies that, except for the brief moment of the actual step in potential, the ion channel is always at or near an equilibrium state.

Recently, a new approach to protocol design was described (Millonas & Hanck, 1998a, 1998b), which proposed the use of rapidly fluctuating voltage pulses rather than the stepped-potential protocols, through a method called *Nonequilibrium Response Spectroscopy* (NRS). By the use of NRS pulses, the protein molecule is continuously driven by a fluctuating electric field, hence it might end up in a highly nonequilibrium configuration, unreachable by currently used experimental methods. Henceforth, when recording the response of the system under these conditions, new information can be attained as the channel is observed under nonequilibrium conditions, rather than at its equilibrium state. The nonequilibrium currents are a qualitatively different set of data (different from currently recorded relaxation transients) and put additional constraints on the Markov models proposed, thus reducing the number of DMMs consistent with the data. It is hoped that the application of the NRS technique to ion channel modeling may provide a means of resolving some of these modeling ambiguities.

A more abstract geometric argument in favor of the NRS technique has been given as well (Millonas & Hanck, 1998a). If we assume that n gross conformational states are required to sufficiently describe the channel kinetics, the space of all these possible conformational distributions is a manifold that we call a *kinetic manifold*. A state of an ion-channel molecule can be described as a point in this n-dimensional space. When we study the channel using stepped potentials, we begin in an initial equilibrium state. During the step, the channel briefly jumps away from this equilibrium state but soon returns to a new equilibrium, since the potential is held for a relatively long time, as described above. Thus, with the use of stepped-potential protocols, the channel always remains near a one-dimensional submanifold of equilibrium states, the *equilibrium submanifold*. This, therefore, implies that with the stepped potential protocols the entire kinetic manifold is hardly being explored. In other words, only a very small (large codimension) subset of the set of all possible states of the molecule is being observed and explored. This is the main source of ambiguities in the modeling process.

Pulses designed for the NRS method can be of two forms, an ensemble of waveforms or single complex waveforms (Kargol et al., 2002). Using the ensemble NRS pulses, the average response of the channel is measured for a set of random waveforms from a statistical ensemble with given properties, whereas with the single complex NRS pulses, the response of the channel is recorded for one single pulse. There have been studies comparing different Markov models for the *shaker* potassium channel using ensemble NRS pulses in the form of dichotomous noise (Kargol, 2002) as well as other NRS pulses in the form of simple oscillating sine waves (Kargol, Hosein-Sooklal, Constantin & Przestalski, *unpublished observations*). In this paper we aim to show how single complex NRS pulses can be used to distinguish between two different models for the human heart isoform of the sodium channel. The protocols used are based on custom-designed single complex waveforms that produce different model responses. We

introduce a new technique of analyzing and comparing the ionic current data obtained from experiments and model responses using these new pulse protocols, through the use of wavelet transforms. The models are compared to the experimental data both qualitatively and quantitatively.

Materials and Methods

Cell Culture, Maintenance and Preparation

A human heart isoform of the sodium channel (hH1a) stably expressed in HEK293 cells was used in the study. The cells were cultured in 35-mm dishes in Dulbecco's Modified Eagle's Medium (DMEM) containing 10% fetal bovine serum, 200 μl G418 and 1 ml/100 ml penicillin-streptomycin and kept at 37°C (5% CO_2). In preparation for experiments, the cells were released using 250 μl trypsin with EDTA, washed and suspended with 600 μl growth medium (DMEM). All reagents used were from Gibco BRL, Gaithersburg, MD, except penicillin/streptomycin (Cellgo, Herndon, VA) and G418 (geneticin) (BioWhittaker, Walkersville, MD).

Recording Technique

Low-resistance pipettes of borosilicate glass were pulled using a Sutter 97 micropipette puller (SDR Clinical Technology, Middle Cove, NSW, Australia). Tips were typically fire-polished into a rounded shape (Millonas & Hanck, 1998a). Pipette resistance normally ranged from 500–800 kΩ. The recording apparatus consisted of an Axopatch 200B amplifier with a CV 203 BU headstage (Axon Instruments, Union City, CA). The headstage was connected to the extracellular solution using a 3 M KCl agar bridge and the recording apparatus set for whole-cell recording. Experiments were performed at 12°C using a Physitemp temperature control system (Physitemp Instruments Inc., Clifton, NJ). During experiments, seals of around 1 GΩ were routinely obtained.

The voltage protocols used consisted of both stepped potentials, which were prepared using the templates in a Pulse program (Heka Electronik, Lambrecht, Germany), as well as custom-designed pulses generated as binary files using MATLAB (Mathworks, Natick, MA) routines. The programs ran on a Pentium II 450 MHz Gateway computer (Gateway Inc., San Diego CA).

The data was filtered at 10 kHz on an analog filter and digitized at 200 kHz using the ITC18 AD/DA converter (Instrument Corp., Great Neck, NJ) and stored on a disk.

Solutions

Extracellular and intracellular solutions were prepared as described by Millonas & Hanck (1998a). The extracellular solution contained in mM: 100 NaCl, 304 MES, 200 CsOH, 2 $CaCl_2$ and 10 HEPES (pH 7.37). Intracellular solution contained in mM: 10 NaCl, 284 CsF, 10 CsCl and 10 HEPES (pH 7.4). The voltage was corrected so that the offset would be zero in the bath before sealing the pipette to the cell. This offset potential was normally ≤3 mV.

Experimental Protocols

Stepped Potentials

The designed stepped-voltage protocols, using the templates available in the Pulse program, were the standard-activation and tail protocols together with steady-state inactivation protocols. For the activation protocol, the transmembrane voltage was set to −130 mV, then increased to 54 mV in voltage increments of 8 mV. The new potential was held for 40 msec and the transient current response recorded before returning to the holding potential. Leak and capacity transients were corrected using the P/4 method with potentials not exceeding −102 mV. For the tail protocols, the depolarizing potential was set to 32 mV for 1 msec, then repolarized to a series of potentials from −150 mV to 18 mV with voltage increments of 12 mV. This repolarized potential was held for 10 msec and currents were recorded before returning to −150 mV. Similar copies of the pulse were also created for capacity correction and leak subtraction using the P/4 method as in the activation protocol. Steady-state inactivation protocols were designed to track the spontaneous hyperpolarizing shift in the Na^+ channel kinetics, which have been shown to occur during voltage-clamp recordings (Hanck & Sheets, 1992). The protocol for the steady-state inactivation involves stepping the membrane from a holding potential of −150 mV to a conditioning potential between −150 and −40 mV for 750 msec, followed by a step to a positive potential of 30 mV for 25 msec, where the current-transient response was recorded. The potential shift was computed using the half-point voltage of a Boltzmann distribution fit to the steady-state inactivation as a measure relative to the half point upon breaking into the cell. The $V_{1/2}$ value was found to be −98 mV on the average from the cells measured.

Single Complex Waveforms

The NRS pulses were designed to produce different responses of the models in the study. These pulses belonged to a different class from those considered by Millonas and Hanck (1998a). In that paper, an ensemble of rapidly fluctuating pulses in the form of dichotomous noise was used and an average channel response determined. However, here we concentrate on the design of a single voltage waveform, using a pulse design strategy outlined by Kargol et al. (2002), where a pulse design algorithm based on a wavelet basis was described.

A mathematical description of the wavelet theory was presented as an appendix (Kargol et al., 2002) and a more detailed information on the subject is available (Daubechies, 1992; Aldroubi and Unser, 1996). For the sake of completeness, we present here a brief introduction to wavelets.

The idea of wavelets originated in signal processing, where there was need for both temporal and spectral information. Standard analysis methods like the Fourier transform provide information only about spectral composition of a signal. A wavelet is a function that performs few rapid oscillations but is zero otherwise. An example, a Daubechies 8 wavelet used in our study, is shown in Fig. 1*a*.

Wavelet analysis is similar in many ways to Fourier analysis, where a superposition of basis functions is used to approximate a signal. However, in Fourier analysis the basis functions used are sine and cosine functions. These basis functions are multiplied by coefficients that can change the amplitude and phase and, when summed together, the signal is reproduced. The Fourier transform of a signal provides information about the frequencies contained in the signal without information of when these frequencies occurred. Even with the use of *windowed Fourier transform*, where, instead of expanding the entire signal into an infinite sum of sines and cosines, a short-time *window* is used and a segment of the signal is compared, there are certain compromises. If too short a time window is chosen, although there is good time resolution as sudden changes and discontinuities are observed, lower-frequency components of the signal cannot fit in the window, resulting in poor resolution of these frequencies. If too long a window is selected, there is good

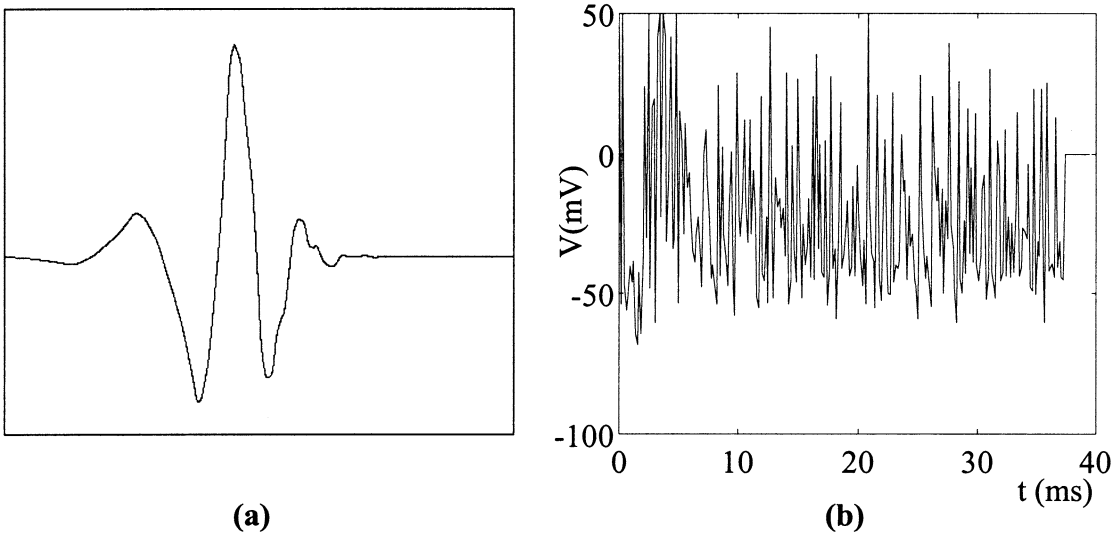

Fig. 1. (*a*) The Daubechies 8 (db8) wavelet. This wavelet was used to build the complex single-voltage pulses. (*b*) A plot of amplitude versus time for the VI7 pulse, one of the pulses created using the db8 wavelet.

resolution of the low-frequency components but poor resolution in time. With wavelets, the problem is reduced, as it is possible to analyze a signal in both time and frequency with relative accuracy, through the use of analyzing functions with finite domains. These approximating functions are called *analyzing wavelets* or *mother wavelets*.

Dilations and translations of the *analyzing wavelet* $\Psi(t)$, define a basis (the wavelet basis), which for certain families of wavelets can be orthonormal. A special case is the so-called *dyadic wavelet basis*, which consists of wavelets dilated by powers of 2 and translated by integers. A member of such basis obtained from the mother wavelet Ψ has a form:

$$\psi_{m,n}(t) = 2^{\frac{-m}{2}}\Psi(2^{-m}t - n) \tag{1}$$

where integers m and n are the scale and translation parameters.

The scale index m indicates the wavelet's width and the location index n gives the position. Positive values for m result in stretched, slowly oscillating copies of the mother wavelet, while negative values of m result in compressed fast-varying versions. The former can be used in analyzing low-frequency components of the signal, while the latter are suitable for analysis of the high-frequency components. When the signal is expanded into a super-position of basis wavelets, the wavelets with the same value of dilation parameter form a level containing signal details on that scale. Translated wavelets within the same resolution level give information about temporal properties of the signal. A set of coefficients of this expansion is known as the wavelet transform. The level structure of the wavelet transform bears the name of *multiresolution analysis*. In other words, the signal is decomposed as the sum of levels containing details in a given frequency range determined by the properties of the mother wavelet and the dilation parameter for the level. Thus, by using wavelets with different indices, information about the spectral composition of a signal at different times can be obtained.

For a discretely sampled signal, the use of the discrete wavelet transform (DWT) produces a mapping from one set of discrete numbers (the signal) to another set of discrete numbers (the coefficients in the expansion). Using the reverse method (the inverse discrete wavelet transform IDWT), we can take a set of coefficients $d_{\mathrm{m,n}}$ to reproduce the signal:

$$f(t) = \sum_{\mathrm{m,n}} d_{\mathrm{m,n}}\psi_{\mathrm{m,n}}(t) \tag{2}$$

Our pulse-search algorithm (Kargol et al., 2001b) is based on reconstructing a voltage pulse from a set of wavelet expansion coefficients by means of the IDWT. It begins with a randomly selected set of wavelet coefficients for which the IDWT yields the initial pulse, according to equation (2). By random perturbation we generated a number (we typically used 10) of next generation wavelet coefficient sets and reconstructed corresponding test pulses. One of these was selected as the starting point for the following generation and the process is repeated for a number of times (500 per coefficient was typically sufficient). To ensure the convergence of this process, the range of the perturbations leading to next generation trial sets decreased according to:

$$r_{\mathrm{i}}(k+1) = r_{\mathrm{i}}(k)(1 + \sigma_{\mathrm{ik}}\exp(-Rk)) \tag{3}$$

where: $r_{\mathrm{i}}(k)$ is the i-th wavelet coefficient at generation k, σ_{ik} are uniform random variables in the interval $-\Delta \le \sigma_{\mathrm{ik}} \le \Delta$ with $0 \le \Delta \le 1$, and R is the rate of decrease of the search radius. In trials with 10,000 generations we used $R = 0.0003$.

At each generation, the selection of one of the test pulses was based on its ability to differentiate between two ion channel Markov models studied. To this end, DMM responses (model currents I) were computed for each of the test voltage pulses, their difference quantified according to:

$$\chi^2 = \frac{\Sigma(I_{\mathrm{model1}} - I_{\mathrm{model2}})^2/I_{\mathrm{model1}}}{\#\text{sampling points}} \tag{4}$$

and the pulse maximizing χ^2 selected. The pulse amplitude was also varied. Amplitudes used were 140 mV, 170 mV and 200 mV and the pulses called V14, V17 and V20, respectively. A typical run of the algorithm took around 12–14 hours on a Pentium III 450 MHz processor. A sample pulse generated for use in this study is shown in Fig. 1*b*.

Data Analysis

Programs used to analyze the data were written in MATLAB. To ensure sufficient bandwidth of the recording apparatus, the relaxation time constant was determined from the capacity transients

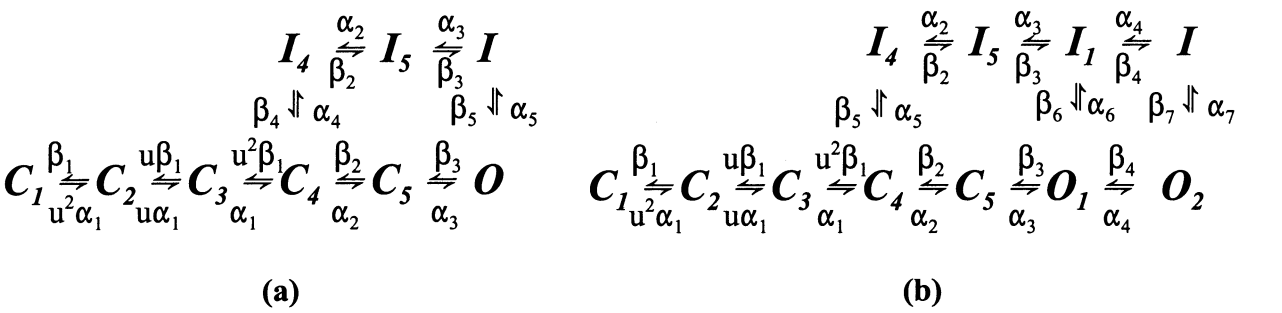

Fig. 2. (*a*) The Vandenberg-Bezanilla model for the sodium channel. (*b*) The Millonas-Hanck model for the sodium channel. This model is a modified form of the Vandenberg-Bezanilla model proposed to improve the fit to experimental data. *C*, *O*, and *I* represent the closed, open and inactivated states, respectively. Reproduced from Millons & Hanck, 1998a, with permission.

recorded in response to a voltage step. Only the cells with a bandwidth of at least 8 kHz were used in the analysis. This corresponds to a time constant of not more that 20 μsec. The cell capacitance was obtained by integrating the capacity transient response to a series of step potentials from a holding potential of −130 mV. The data was capacity-corrected using standard methods.

The Models

The two models studied were the Vandenberg-Bezanilla model (Vandenberg & Bezanilla, 1991a, 1991b) shown in Fig. 2*a* and the Millonas-Hanck model (Millonas & Hanck, 1998a) in Fig. 2*b*. The Vandenberg-Bezanilla model was based on the results of a series of experiments on single-channel, macroscopic ionic and gating current. The basic features of the model include (i) a series of closed states in the activation pathway, (ii) a set of inactivation states in parallel to the activation states, (iii) possible inactivation from both the open and closed states, which is reversible. This model allows both activation and deactivation to proceed along the same pathway. The Millonas-Hanck model consists of similar topology as the Vandenberg-Bezanilla model, except for additional open and inactivation states added to the model. This final model was proposed by Millonas and Hanck (1998a), because it produced a better fit to the macroscopic ionic current measured in their experiments with stepped potential protocols.

Theory of Markov Models

The kinetic scheme of a discrete Markov model describes the possible conformational states of the protein and transitions among them when a given activating potential is applied (in case of voltage-gated channels). Two examples, used in this work, are shown in Fig. 2. The transition rates between the states are voltage dependent and assumed to have the standard Eyring form (Eyring, 1935):

$$\alpha_i(V) = \alpha_i(0)\exp\left(q_i\delta_i\frac{V}{kT}\right) \tag{5}$$

$$\beta_i(V) = \beta_i(0)\exp\left(-q_i(1-\delta_i)\frac{V}{kT}\right) \tag{6}$$

where $\alpha_i(0)$ and $\beta_i(0)$ are the activation rates at zero voltage, q_i are the gating charges, while $0 < \delta_i < 1$ is a dimensionless parameter representing fractional electrical distances; V is the voltage in mV, k is the Boltzmann constant and T, the absolute temperature. Since each of these models possesses closed loops, the principle of microscopic reversibility is used (Läuger et al., 1980). This basically dictates that the product of the transition rates in any one direction must be equal to the product of the transition rates in the opposite direction around the same closed loop. In this case, certain adjustments were made for this relationship in the two models. For the Vandenberg-Bezanilla model, the principle of microscopic reversibility dictated that $\alpha_5\beta_4 = \alpha_4\beta_5$, the constraint applied to the system was then $\beta_4 = \alpha_4\beta_5/\alpha_5$. In the case of the Millonas-Hanck model, there exist two closed loops. Thus, the principle of microscopic reversibility dictated that $\alpha_7\beta_6 = \alpha_6\beta_7$ and $\alpha_6\beta_5 = \alpha_5\beta_6$, which enforced the following two constraints: $\beta_6 = \alpha_6\beta_7/\alpha_7$ and $\beta_5 = \alpha_5\beta_7/\alpha_7$, respectively.

For each model, the parameters were used to calculate the transition matrix, **W**. The probability vector, $\vec{P}$ (i.e., the vector of probabilities of the channel being in any one of the conformational states of the model), is computed from the kinetic master equation:

$$\frac{d\vec{P}(t)}{dt} = \mathbf{W}\vec{P}(t) \tag{7}$$

The formal solution to this equation can be written as:

$$\vec{P}(t) = \exp(\mathbf{W}t)\vec{P}_0 \tag{8}$$

where $\vec{P}_0$ is the initial probability vector. It can be calculated using standard matrix routines in MATLAB. For the step potentials, the transition matrix **W** is time independent. However, for the time-varying pulses it becomes time dependent as a direct result of the dependence of the transition rates on the voltage. Thus, a formal solution to equation (6) then becomes:

$$\vec{P}(t) = \exp\left(\int_0^t \mathbf{W}(s)ds\right)\vec{P}_0 \tag{9}$$

The explicit form of the equation is determined by an iteration with a time step equal to the voltage sampling rate. The initial probability vector $\vec{P}_0$ is determined by solving equation (8) with the transition matrix corresponding to the holding potential and a sufficiently long t to ensure complete equilibration at this voltage.

The model current can be calculated using the following equation:

$$I(t) = g_0 g(V)(V - V_r)\vec{O}\cdot\vec{P}(t) \tag{10}$$

where $\vec{O}$ is the projection vector onto open states so that the total probability of the channel being open is $\vec{O}\cdot\vec{P}$. V_r is the reversal potential, which is determined from the instantaneous current-voltage relationship of the channel-activation data. The polynomial $g(V)$ is the nonlinear instantaneous conductance, which is determined from the tail current data. Thus, for any given cell used in the analysis, the reversal potential and nonlinear conductance are

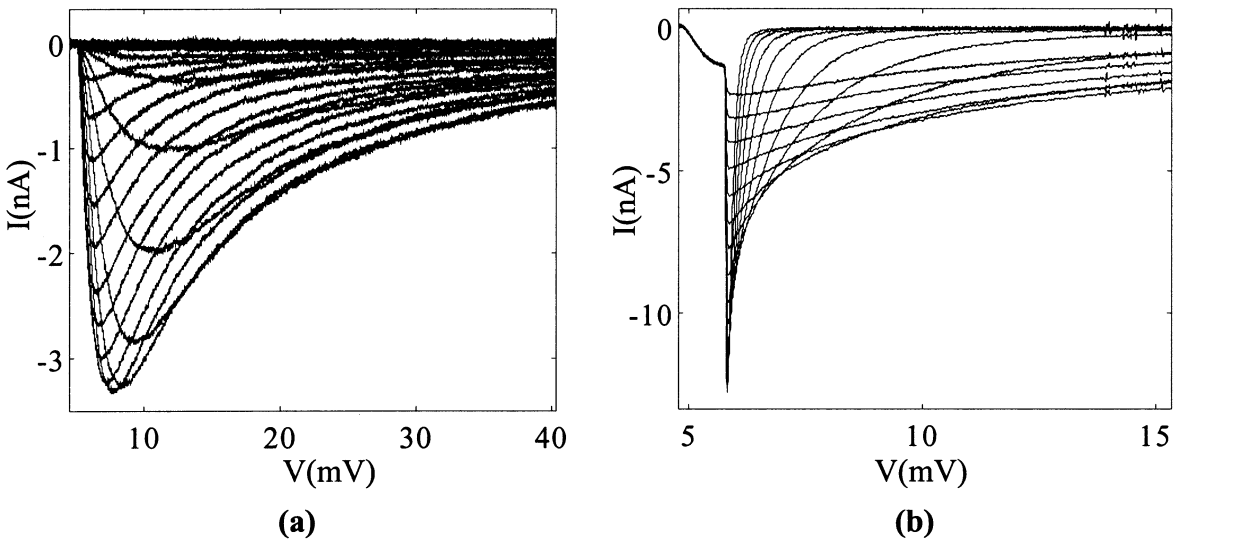

Fig. 3. (*a*) Activation data obtained from whole-cell recording for 24 sweeps from a holding potential of −130 mV with increments of 8 mV. (*b*) Tail data obtained from whole-cell recording for 15 sweeps. The cell was initially depolarized to 32 mV, then repolarized from −150 mV in increments of 12 mV.

determined from the experimental data. These values are used when trying to fit the kinetic model to the experimental data.

Model Fitting

The parameters of each of the models were determined using a simulated annealing algorithm, similar to that described earlier (Millonas & Hanck, 1998a). This algorithm involves a random search in parameter space with a decreasing search radius. For each model, we begin with a set of randomly chosen model "parent" parameters. By selecting the number of generations, the rate of annealing (rate of decrease of the search radius) and the number of variations of the parameters we would like, a set of new random parameters (seeds) are generated. The model response (the model current) is computed for each test model and the set with the best fit to the experimental data becomes the "parent" set for the next generation. The average run of about 500 generations took about 4–7 hours on a Pentium III, 450 MHz processor. The number of variations were set at 10 with an annealing rate of 0.0075.

Results and Discussion

Stepped-Potential Protocols

The responses to the stepped potentials applied across the cell membrane during measurement of channel activation and tail ionic currents were first analyzed for each cell used in the study. Figures 3*a* and 3*b* show typical activation and tail-current data obtained from our experiments after capacity correction and leak subtraction.

The peak activation current measured for each stepped potential was determined and plotted. This curve was used to determine the activation potential, Fig. 4*a*. The graph shows the activation voltage for the sodium channel around −70 mV and the reversal potential of 60 mV. These values are consistent with the values reported by Millonas & Hanck (1998a) for the same channel. The conductance transform of the peak current was calculated using Ohm's law ($I = Vg$), where I is the peak measured current, V is the voltage difference between the applied voltage and the reversal potential ($V = V_{\text{applied}} - V_{\text{r}}$) and g is the conductance to be calculated. The fractional conductance was determined and a normalized plot produced, taking into account the measured instantaneous voltage dependence and shift (the shift in voltage during the activation protocol), which was determined experimentally to be −18 mV with a slope factor $s = 9.6$ mV, *see* Fig. 4*b*.

The data from the tail current measurements were used to assess voltage control, by plotting the resulting current transient near the time of the voltage change (Fig. 4*c*). The current typically settled to its new value between 30–60 μsec, which was indicative of good control of the voltage across the cell membrane (Millonas & Hanck, 1998a). Figure 4*d* is a plot of the instantaneous conductance obtained from measurements using the instantaneous current-voltage relationship of the tail protocol. The data was made to fit a third-order polynomial in V (Table 1). This polynomial form of $g(V)$ was used in equation (10) to compute and compare the model responses for the activation and tail currents to the experimental data during the optimization for the transition rate parameters and the conductance g_0. The latter is a constant factor dependent on the number of channels in the cell and one that could vary from cell to cell. In order to compute the differences between the experimental data and the models, χ^2 error calculations were performed. This error was normalized to the

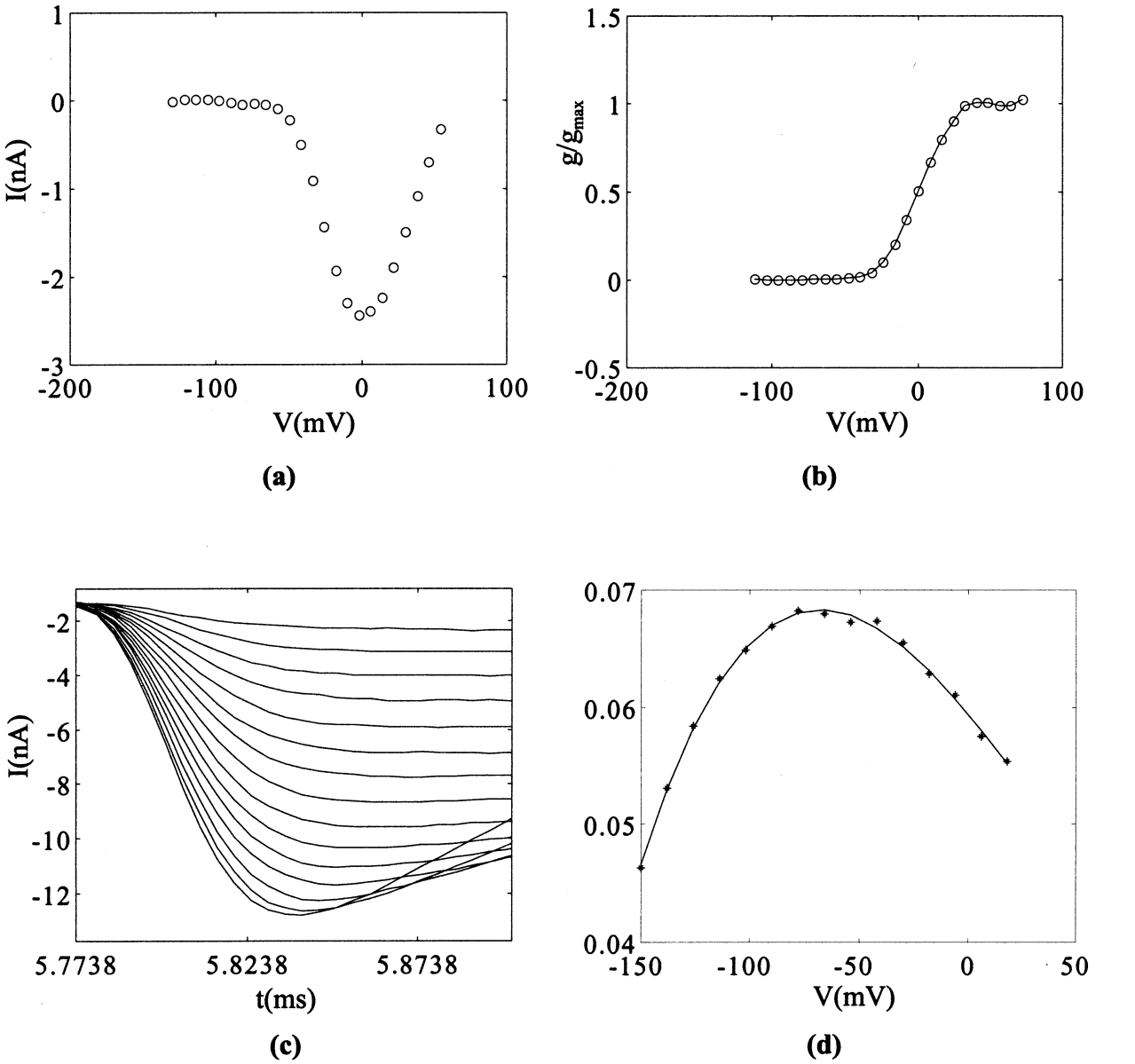

Fig. 4. (*a*) Peak current versus voltage for the activation data. (*b*) Fractional conductance taking into account the measured instantaneous voltage dependence and shift with $V_{1/2}$ determined to be −18 mV. (*c*) Resultant current transient near the time of the voltage change to determine good voltage control. (*d*) Instantaneous conductance fit to a third-order polynomial in V (in mV), here $g(V) = g_0 + g_1 V + g_2 V^2 + g_3 V^3$.

number of traces and the sampling rate. We used an equation analogous to equation (4) but modified by dividing over the number of sweeps in the protocol (24 sweeps for the activation protocol and 15 sweeps for the tail protocol). Table 1 shows the results of the parameter optimization obtained for these stepped protocols for both models.

A typical fit is shown in Fig. 5*a* and 5*b* for the Vandenberg-Bezanilla model and Fig. 5*c* and 5*d* for the Millonas-Hanck model. The plots show that the models were equally successful in matching the experimental data from the stepped potential with certain accuracy. The average χ^2 error calculated for both fits was between 0.3–1.9 pA.

Single Waveform Pulses

Figure 6*s* shows typical experimental data (the signal) from the V17 pulse (all the pulses used in the analysis consisted of similar random features) after leak subtraction and capacity correction using the P/2 method. The data shown is an average of 100 sweeps.

The signals obtained from the experiment and the model responses were analyzed using discrete wavelet

Table 1. Optimal model parameters for the Vandenberg-Bezanilla model and the Millonas-Hanck model where $u = 1.2$

Vandenberg-Bezanilla				Millonas-Hanck			
α (sec^{-1})	β (sec^{-1})	δ	q (units of e)	α (sec^{-1})	β (sec^{-1})	δ	q (units of e)
5745.8	10.9	0.0189	2.1516	14146.8	1.4×10^{-5}	0.0162	1.9421
4237.1	24.3	0.6194	2.9110	2962.5	9.8	0.5498	3.3941
664.2	3477.0	0.3017	0.0771	1768.5	3425.5	0.6892	0.0034
25.1	1.9	0.0774	6.5569	62.5	58.8	0.1524	1.2362
987.0	86.6	0.1853	0.1034	8.2	6.4	0.3734	0.6307
				313.9	245.6	0.3486	0.0537
				2639.6	2.4	0.0439	0.7258
$g_0 = 7.4967$				$g_0 = 3.0928$			
$g(V) = (-9.2202 \times 10^{-10})V^3 + (-3.0286 \times 10^{-6})V^2 + (-3.6302 \times 10^{-4})V + (-0.0580)$							

Also shown are the optimized constant conductance g_0 and $g(V)$, the instantaneous conductance determined from measurements of the instantaneous current-voltage relationship of the tail protocol.

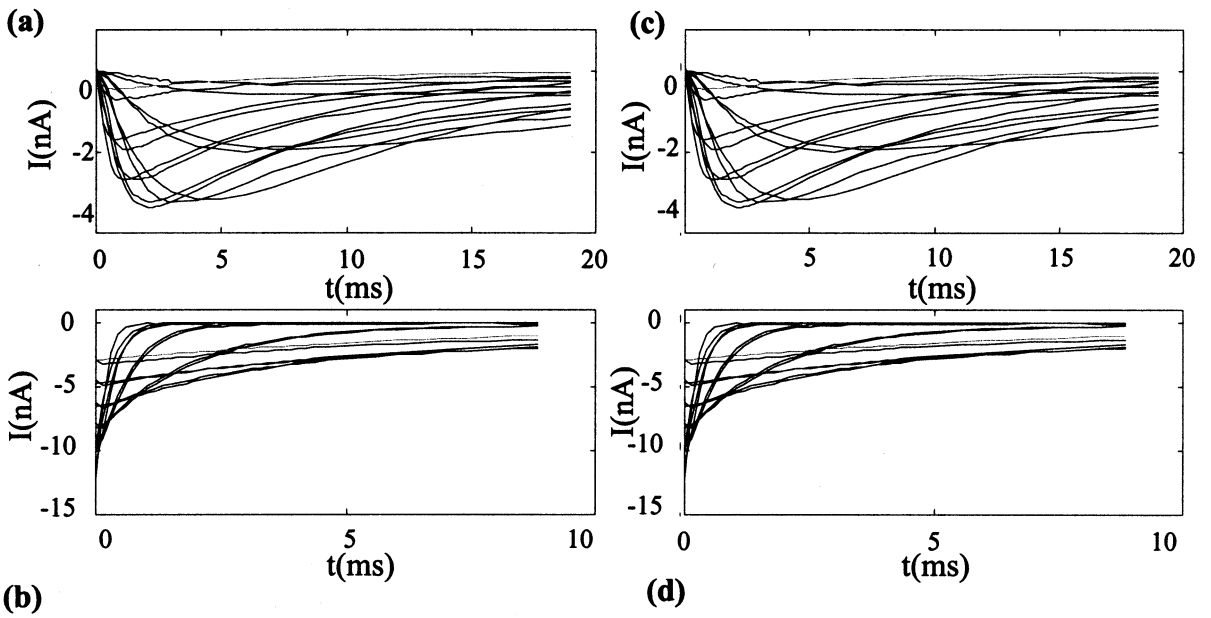

Fig. 5. Fits of the two models to the experimental data from stepped potentials. (*a*) Vandenberg-Bezanilla fit to activation series. (*b*) Vandenberg-Bezanilla model fit to tail series. (*c*) Millonas-Hanck model fit to activation series. (*d*) Millonas-Hanck model fit to tail series.

transform (DWT). As we explained in the Methods (Single Complex Waveforms), the DWT analyzes the signal at various levels with the time scale matched to the frequency content. This is done by means of decomposing the signal into a coarse approximation and the detail information, through the use of low-pass and high-pass frequency filters, respectively. When the signal with maximum frequency f passes through the filters, the frequencies are separated into those that are more than half the highest frequency and those that are less than half the highest frequency of the original signal. The signal is then subsampled by 2, leaving half the original number of points. The output of the first high-pass filter consists of the higher-frequency components and constitutes the coefficients of the first level of decomposition, while the signal output of the low-pass filter consists of the lower-frequency components with maximum frequency of the low pass-filtered signal being $f/2$. This low pass-filtered signal then passes through the same high- and low-pass filters for another level of decomposition, where the frequency is again reduced by 2. Here, the second high pass-filtered signal constitutes the coefficients of the second level of decomposition, while the low pass-filtered signal passes through the filters for further decomposition. Decomposition can continue until only 2 points remain. The frequency decreases by 2 for each level of the decomposition. This implies that *DWT coefficients at low levels correspond to the high frequencies, whereas DWT coefficients at high levels correspond to low frequencies*.

Using the discrete wavelet transform, the signal was decomposed into Approximation and Detail coefficients for each level (Fig. 6(a_1–a_8) and (d_1–d_8),

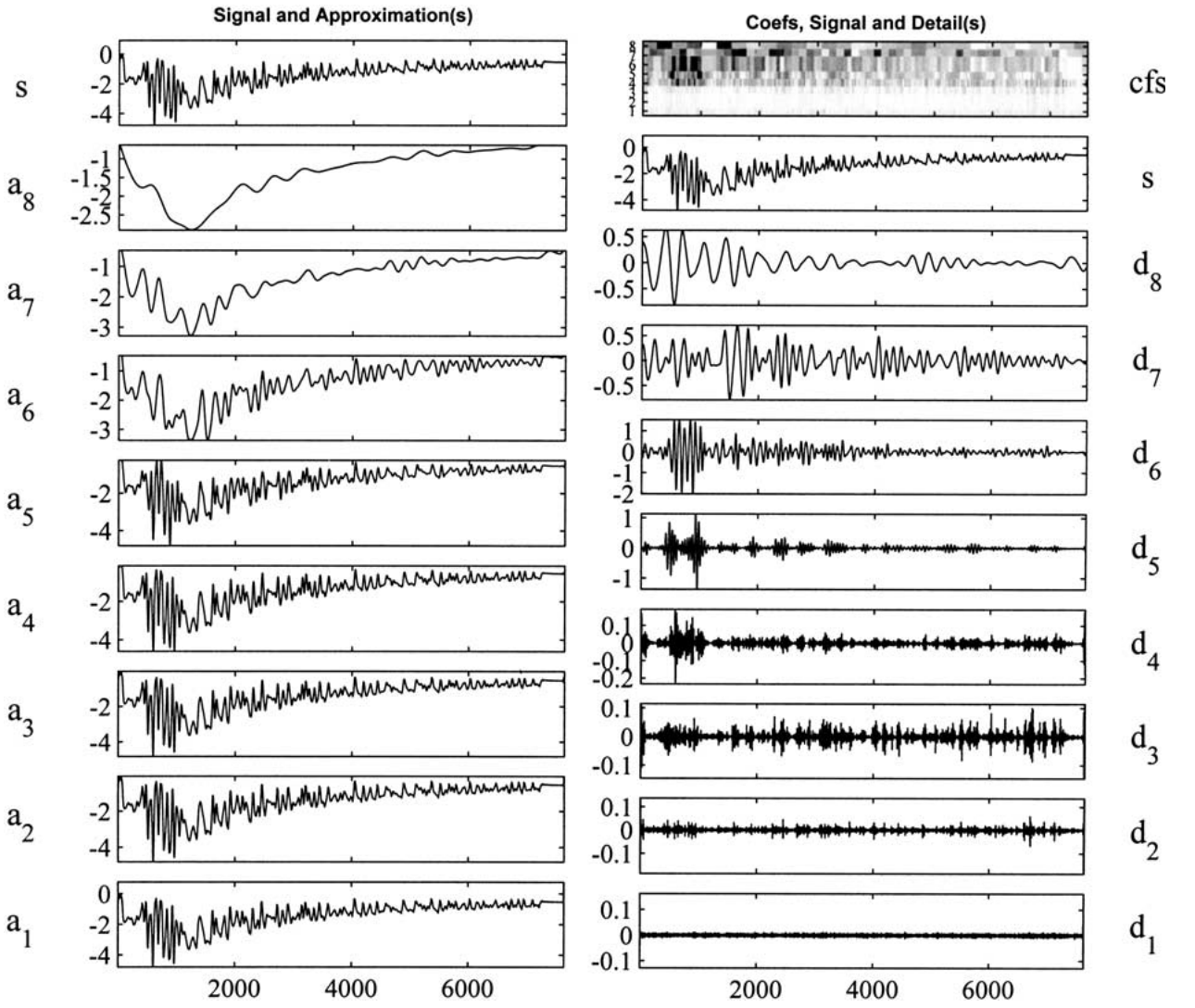

Fig. 6. Wavelet decomposition analysis on experimental data obtained from V17 pulse. (*s*) The actual signal as obtained from experiment. (a_1–a_8) The approximation coefficients obtained during the decomposition up to level 8. (d_1–d_8) The detail coefficients obtained during the decomposition up to level 8. (*csf*) The coefficient levels.

respectively). Graphs (a_1–a_8) show coarser and coarser approximations to the signal, with the higher approximation number corresponding to a coarser approximation (lower-frequency components). The graph shown does not show a full wavelet expansion of the signal. The approximation (a_8) can be further decomposed into yet lower frequency components. Graphs (d_1–d_8) show the detail at a given level, i.e., the difference in passing to a coarser approximation. The complete signal can be recovered as a sum of the coarsest approximation and all details at various levels, i.e., for the example shown in Fig. 6:

$$s = a_8 + d_8 + d_7 + d_6 + d_5 + d_4 + d_3 + d_2 + d_1 \qquad (11)$$

Fig. 6*cfs* shows the coefficients of the wavelet expansion. Further analysis of this pulse as well as the V14 and V20 pulses are shown in Figs. 7, 8 and 9.

To qualitatively compare the signals, plots were made of the coefficients of the signal obtained from the experiment, the Vandenberg-Bezanilla model and the Millonas-Hanck model for the different pulses investigated. Figure 7 shows the plots for the V14 pulse including all levels of the wavelet decomposition. The differences in the model behavior compared to the experimental results is visually obvious, with the absolute value of the coefficients being expressed on the gray scale (the darkest = the largest coefficient). First noticeable is the fact that the experimental signal contains essentially no components at levels 1–3, i.e., at the highest frequency range. This does not come as a surprise, since the signal has been filtered at 10 kHz and the recording bandwidth of our apparatus is limited, too. In contrast, the model currents have no such limitation, which is especially apparent for the Millonas-Hanck model. The rela-

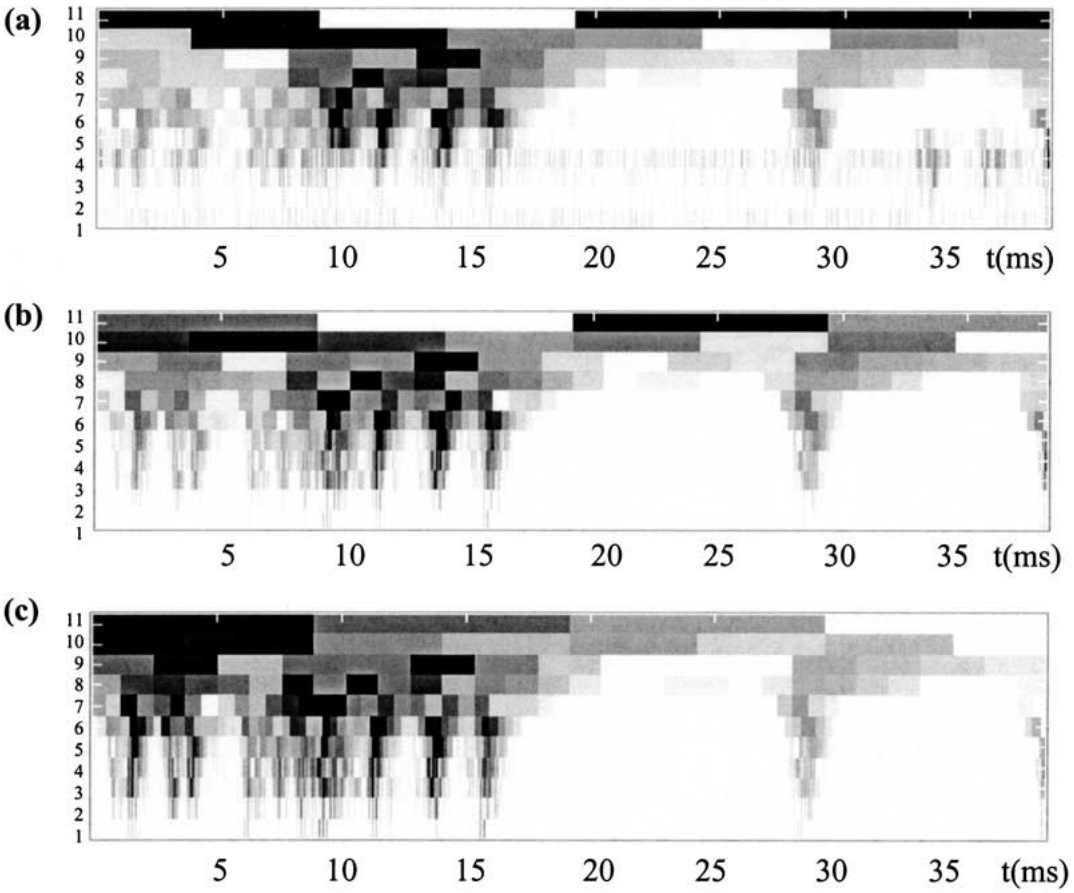

Fig. 7. Comparison plots of the detail coefficients obtained at each level from the decomposition of the experimental signal and the model responses for the V17 pulse. (*a*) Experimental signal. (*b*) Vandenberg-Bezanilla model response. (*c*) Millonas-Hanck model response.

tively weak bands, uniformly distributed throughout the duration of the signal, can be attributed to random noise present in the experimental signal. Although care was taken to eliminate sources of noise in the recording apparatus, and the noise level was further reduced by averaging over a large number of sweeps, the experimental signal at levels 1–3 still shows traces of the random noise. The main feature, however, is the different pattern of the wavelet coefficients. We recall that the horizontal axis corresponds to time, i.e., it determines *when* during the signal a given frequency has appeared, while on the vertical axis we have detail levels (lower frequencies on the top). A noticeable feature in the Millonas-Hanck model is that the signal details at all scales fade away toward the end of the duration of the signal and tend to be more pronounced at the beginning of the signal. The same phenomenon is visible in Figs. 8 and 9, showing responses to pulses V17 and V20, respectively. On the other hand, the Vandenberg-Bezanilla model (Figs. 7*b*, 8*b*, 9*b*) follows the pattern shown in the experimental data (Figs. 7*a*, 8*a*, 9*a*) very closely, both in terms of the temporal distribution and the coefficient value.

A more quantitative measure of the differences of the models was obtained by performing a χ^2 analysis of the wavelet transforms. Here, each model was compared to the experimental data by the χ^2 error equation (equation (4)) for each level. Plots were then made of the χ^2 error versus the level of decomposition for each of the pulses (Fig. 10). In these plots, the lowest level consists of coefficients of the decomposed signal with the highest frequency while the highest level consists of coefficients of the decomposed signal with the lowest frequency. In other words, as the level of decomposition increases the frequency decreases. The error for the Millonas-Hanck model is significantly larger than for the Vandenberg-Bezanilla model. The difference is most pronounced at levels 7–11. The small value of the χ^2 error at lower levels (1–5) can be explained by overall small values of the wavelet coefficients at these levels. That follows both from the limitations of the experimental setup, as mentioned before, as well as from the design of voltage pulses used, which were typically constructed with up to 9 levels and then up-sampled to the desired sampling rate. The difference between the model currents and the experimental results at higher levels (lower fre-

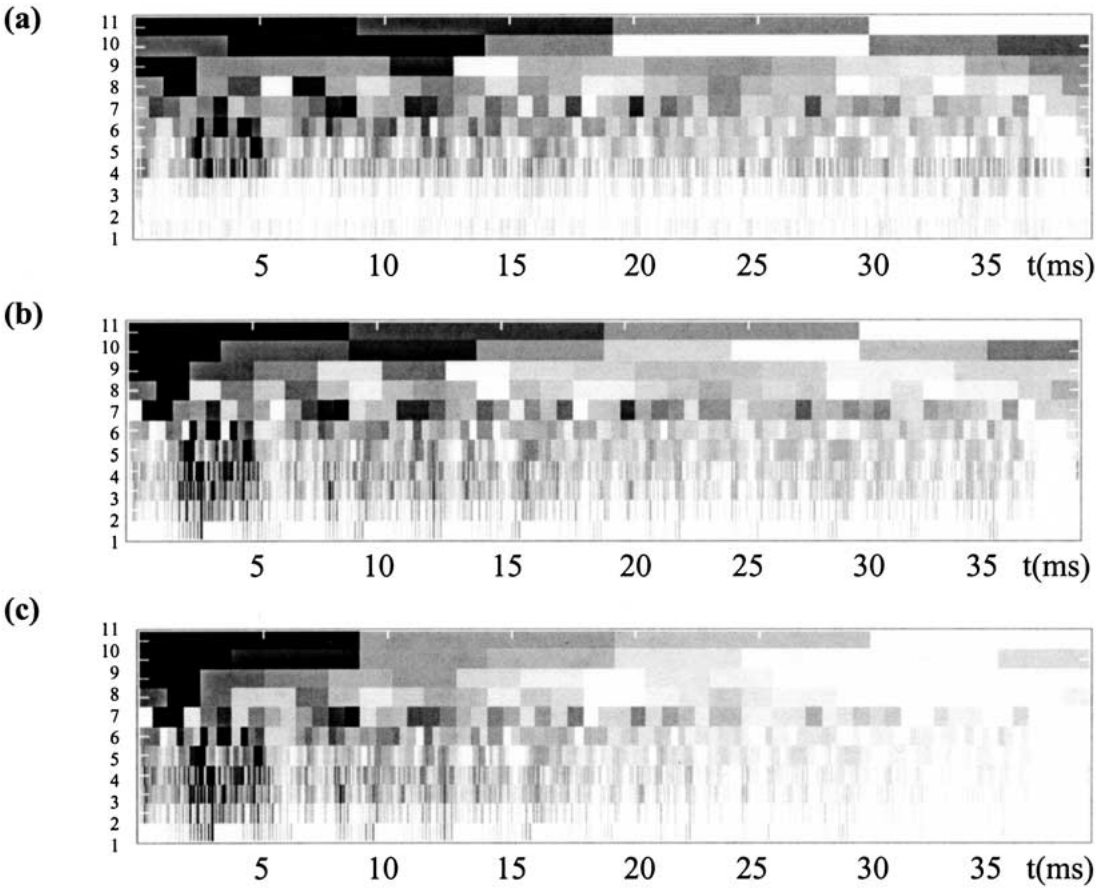

Fig. 8. Comparison plots of the detail coefficients from the decomposition of the experimental signal and the model responses for the V14 pulse. (*a*) Experimental signal. (*b*) Vandenberg-Bezanilla model response. (*c*) Millonas-Hanck model response.

quency range) should not be confused with the claim that the models reproduce well the experimental responses to low-frequency voltage input. The model currents are *not* linear in voltage and even if the voltage input is decomposed into levels of decreasing frequency range, it does not mean that the model currents can be decomposed accordingly. In other words, the lower-frequency current components depend also on higher-frequency voltage levels.

Conclusion

Voltage-clamp protocols with stepped potentials are the standard experimental technique in cell electrophysiology, based on which ion channel-gating kinetics models are built. We studied two models for a sodium ion channel proposed to best describe experimental data from such stepped-potential protocols. In general, a complete model should be able to describe the behavior of the channel under various circumstances. However, models based on stepped-voltage protocols are shown to have certain ambiguities. This is clearly demonstrated from the fact that there may be different proposed models for the ion channel, which are equally successful in reproducing currently available experimental data. It has been argued (Millonas & Hanck, 1998a; Kargol et al., 2002) that these modeling ambiguities stem from inherent limitations of commonly used protocols. When subjected to stepwise voltage changes the ensemble of ion channels undergoes only brief sojourns from an equilibrium manifold and the majority of the kinetic manifold remains unexplored. The method of nonequilibrium response spectroscopy aims at resolving at least some of the mentioned ambiguities in the choice of DMMs for ion channels by exploring far-from-equilibrium regions in the kinetic manifold. This puts additional constraints on the Markov models, thus narrowing the selection field. We designed fluctuating pulses that drive the protein molecule far from its equilibrium state. These pulses were generated using wavelet transform and they were specifically constructed to amplify the difference in responses between the Vandenberg-Bezanilla model and the Millonas-Hanck model.

The results obtained showed that although both models fit the experimental data from the stepped-potential protocols equally well, when the new NRS pulses were applied, there was a distinct

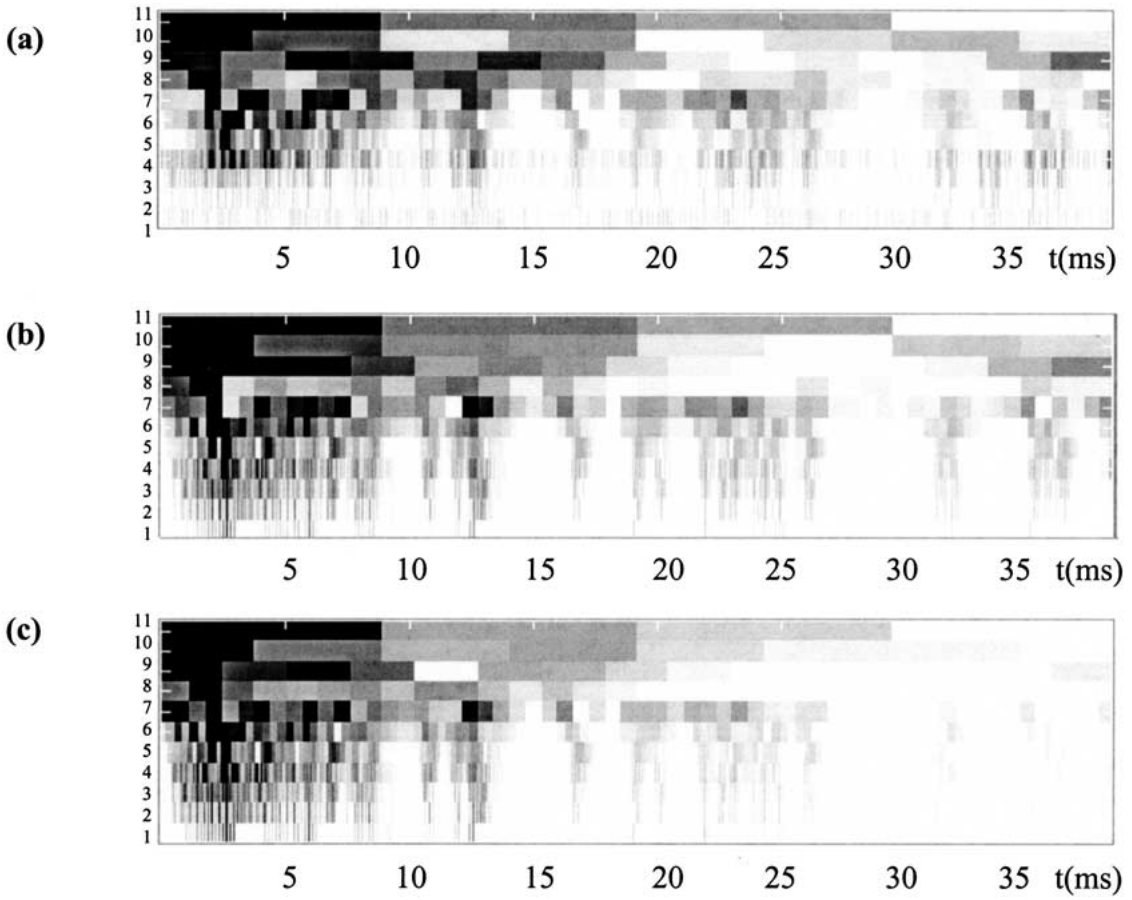

Fig. 9. Comparison plots of the detail coefficients from the decomposition of the experimental data and the model responses to the V20 pulse. (*a*) Experimental data. (*b*) Vandenberg-Bezanilla model response. (*c*) Millonas-Hanck model response.

difference between the way the models responded. We proposed the use of discrete wavelet transform (DWT) to quantitatively analyze the data obtained from experiments and compare it with the current responses of the models. DWT decomposed the signals into levels of varying frequency range and the coefficients obtained from the different decomposition levels were compared. Results showed that while the Millonas-Hanck model displayed certain similarities to the experimental data, the overall differences were greater than the differences of the Vandenberg-Bezanilla model when it was compared to the experimental data. The scale-temporal pattern of wavelet coefficients for the Vandenberg-Bezanilla model was almost identical to the experimental data recorded from hH1A sodium ion channels. The Millonas-Hanck model deviated from the experimental data both in terms of temporal properties of the signal (the wavelet coefficients tended to fade away towards the end of the signal at all resolution scales) and the magnitude of coefficients at different levels.

We concluded that the NRS technique provides means of studying new aspects of ion channel gating kinetics that cannot be attained using the standard stepped-potential protocols. An application of the method is presented here and shown to be successful in distinguishing between two models for a human heart isoform of the sodium channel (Vandenberg-Bezanilla model and the Millonas-Hanck model). By applying custom-designed voltage waveform we showed the Vandenberg-Bezanilla model to be superior. Also, the use of wavelet transform proved to be a very convenient tool in the analysis of experimental data, which were mostly in the form of nonstationary signals (signals with time-varying spectra). To our knowledge, this mathematical tool has never been used in this type of analysis, however, it proved to have potential for further applications in analysis of electrophysiological recordings.

The authors thank H. Hartmann for generously giving to us the stable cell line expressing the hH1A sodium ion channel.

References

Aldroubi, A., Unser, M. (eds.) 1996. *Wavelets in Medicine and Biology*. CRC Press, Boca Raton, New York, London, Tokyo

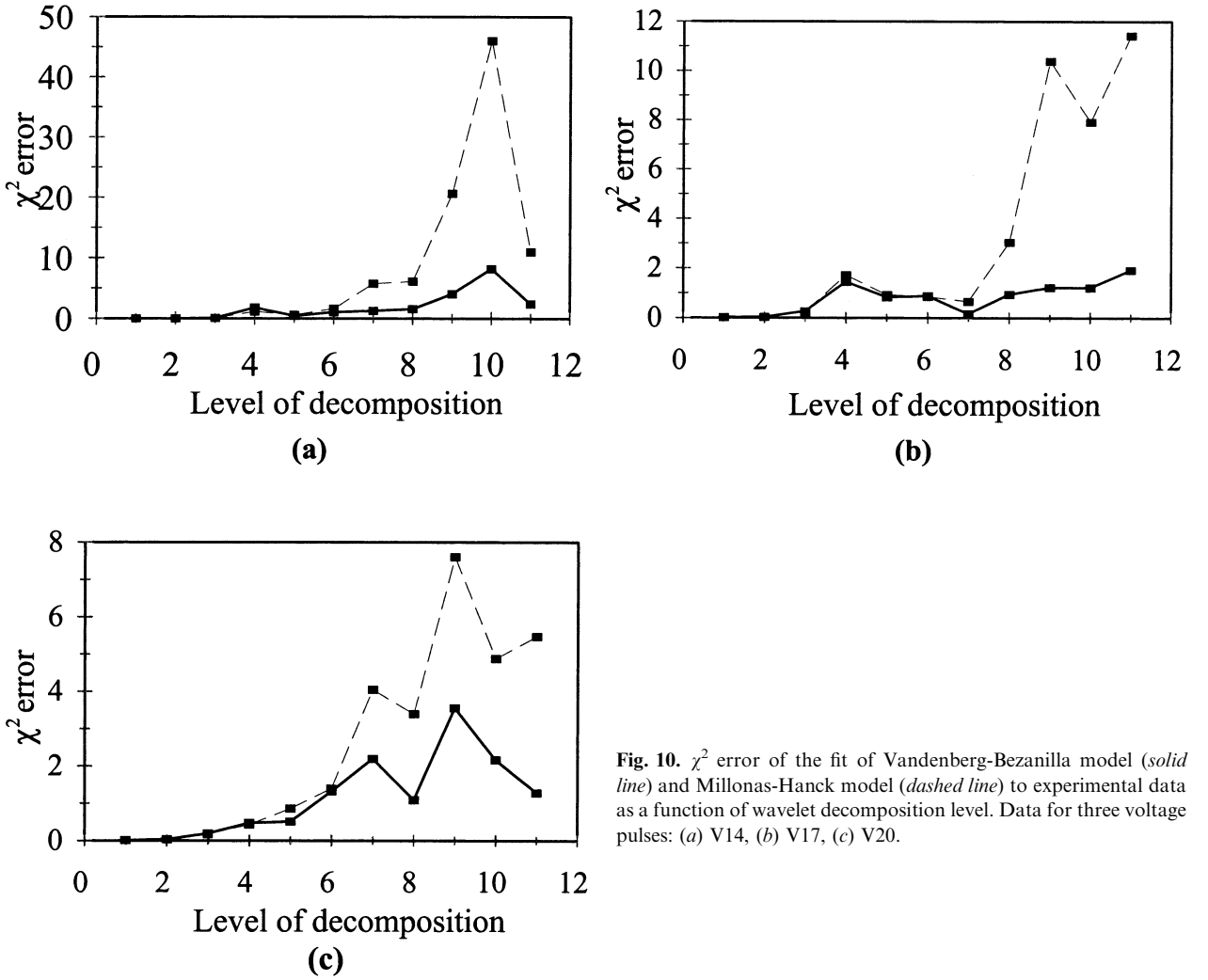

Fig. 10. χ^2 error of the fit of Vandenberg-Bezanilla model (*solid line*) and Millonas-Hanck model (*dashed line*) to experimental data as a function of wavelet decomposition level. Data for three voltage pulses: (*a*) V14, (*b*) V17, (*c*) V20.

Cole, K.S., Curtis, H.J. 1936. Electrical impedance of nerve and muscle. *Cold Spring Harbor Symp. Quant. Biol.* **4:**73–85

Colquhoun, D., Hawkes A.G. 1981. On the stochastic properties of single ion channels. *Proc. R. Soc. Lond. B* **211:**205–235

Daubechies, I. 1992. *Ten Lectures on Wavelets.* SIAM, Philadelphia, PA

Eyring, H. 1935. The activated complex in chemical reactions. *J. Chem. Phys.* **3:**107–115

Fozzard, H., Hanck, D. 1996. Structure and function of voltage dependent sodium channels, Comparison of Brain II and cardiac rms. *Physiol. Rev.* **76:**887–926

Hamill, O., Marty, A., Neher, E., Sakmann, B., Sigworth, F. 1981. Improved patch-clamp techniques for high resolution current recordings from cells and cell-free membrane patches. *Pfluegers Arch.* **391:**85–100

Hanck, D.A., Sheets, M.F. 1992. Time-dependent changes in kinetics of Na^+ current in single canine cardiac Purkinje cells. *Am. J. Physiol.* **262:**H1997–H1207

Hodgkin, A., Huxley, A.F. 1952a. Currents carried by sodium and potassium ions through the membrane of the giant squid axon of *Loligo*. *J. Physiol.* **116:**449–472

Hodgkin, A., Huxley, A.F. 1952b. The components of membrane conductance of the giant squid axon of *Loligo*. *J. Physiol.* **116:**473–496

Hodgkin, A., Huxley, A.F. 1952c. The dual effect of membrane potential on sodium conductance in the giant squid axon of *Loligo*. *J. Physiol.* **116:**497–506

Hodgkin, A.L., Huxley, A.F. 1952d. A quantitative description of membrane current and its application to conduction and excitation in nerve. *J. Physiol.* **116:**507–544

Hodgkin, A.L., Huxley, A.F., Katz, B. 1949. Ionic currents underlying the activity in the giant axon of the squid. *Arch. Sci. Physiol.* **3:**129–150

Hodgkin, A., Huxley A.F., Katz, B. 1952. Measurements of current voltage relations in the membrane of the giant axon of *Loligo*. *J. Physiol.* **116:**424–448

Hoshi, T., Zagotta, W.N., Aldrich, R.W. 1994. Shaker potassium channel gating I: Transition near the open state. *J. Gen. Physiol.* **103:**249–278

Kargol, A., Smith, B., Millonas, M. 2002. Applications of Non-equilibrium Response Spectroscopy to the study of channel gating. Experimental Design and Optimization. *J. Theoret. Biol.* (in press)

Korn, J.S., Horn, R. 1988. Statistical discrimination of fractal and Markov models of single ion channel gating. *Biophys. J.* **54:**871–877

Läuger, P. 1988. Internal motions of proteins and gating kinetics of ion channels. *Biophys. J.* **53:**877–884

Liebovitch, L.S. 1981. Testing fractal and Markov models of ion channel kinetics. *Biophys. J.* **55:**373–377

Liebovitch, L.S., Fischbarg, J., Koniarek, J.P., Todorov, L., Wang, M. 1987. Fractal model of ion channel kinetics. *Biochim. Biophys. Acta* **896:**173–180

Lowen, S., Liebovitch, L.S., White, J.A. 1999. Fractal ion channel behavior generates fractal firing patterns in neuronal models. *Phys. Rev. E* **59:**5970–5980

Marmont, G. 1949. Studies on the axon membrane. I. A new method. *J. Cell. Comp. Physiol.* **34:**351–382

Milhauser, G.L., Salpeter, E.E., Oswald, R.E. 1988. Rate amplitude correlation from single channel records. A hidden structure in ion channel gating kinetics? *Biophys. J.* **54:**1165–1168

Millonas, M., Hanck, D. 1998a. Nonequilibrium Response Spectroscopy of voltage-sensitive ion channel gating. *Biophys. J.* **74:**210–229

Millonas, M.M., Hanck, D.A. 1998b. Nonequilibrium response spectroscopy and the molecular kinetic of proteins. *Phys. Rev. Lett.* **80:**401–404

Neher, E., Sakmann, B. 1976. Single channel currents recorded from membrane of denervated from muscle fibres. *Nature* **260:**799–801

Patlak, J. 1991. Molecular kinetics of voltage dependent Na^+ channel. *Physiol. Rev.* **71:**1047–1077

Schoppa, N.E., Sigworth, F.G. 1998a. Activation of Shaker potassium channels. I. Characterization of voltage-dependent transitions. *J. Gen. Physiol.* **111:**271–294

Schoppa, N.E., Sigworth, F.G. 1998b. Activation of the *Shaker* potassium channels. II. Kinetics of the V_2 mutant channel. *J. Gen. Physiol.* **111:**295–311

Schoppa, N.E., Sigworth, F.G. 1998c. Activation of the *Shaker* potassium channels. III. An activation gating model for wild-type and V_2 mutant channels. *J. Gen. Physiol.* **111:**313–342

Vandenberg, C.A., Bezanilla, F. 1991a. Single channels, macroscopic ionic and gating currents in the giant squid axon. *Biophys. J.* **60:**1499–1510

Vandenberg, C.A., Bezanilla, F. 1991b. A sodium channel gating model based on single channel, macroscopic ionic and gating currents in the squid giant axon. *Biophys. J.* **60:**1511–1533

Zagotta, W.N., Hoshi, T., Aldrich, R.W. 1994a. Shaker potassium channel gating III: Evaluation of kinetic models for activation. *J. Gen. Physiol.* **103:**321–362

Zagotta, W.N., Hoshi, T., Dittman, J., Aldrich, R.W. 1994b. Shaker potassium channel gating II: Transitions in the activation pathway. *J. Gen. Physiol.* **103:**279–319